

Realization of improved efficiency on nanostructured multicrystalline silicon solar cells for mass production

This content has been downloaded from IOPscience. Please scroll down to see the full text.

2015 Nanotechnology 26 125401

(<http://iopscience.iop.org/0957-4484/26/12/125401>)

View [the table of contents for this issue](#), or go to the [journal homepage](#) for more

Download details:

IP Address: 202.120.52.96

This content was downloaded on 09/03/2015 at 03:10

Please note that [terms and conditions apply](#).

Realization of improved efficiency on nanostructured multicrystalline silicon solar cells for mass production

X X Lin^{1,2}, Y Zeng¹, S H Zhong¹, Z G Huang¹, H Q Qian³, J Ling³,
J B Zhu³ and W Z Shen^{1,4}

¹Institute of Solar Energy, Laboratory of Condensed Matter Spectroscopy and Opto-Electronic Physics, and Key Laboratory of Artificial Structures and Quantum Control (Ministry of Education), Department of Physics and Astronomy, Shanghai Jiao Tong University, Shanghai 200240, People's Republic of China

²Department of Mathematics and Physics, Shanghai Dian Ji University, Shanghai 201306, People's Republic of China

³Wuxi Suntech Power Co., Ltd, 9 Xinhua Road, New district, Wuxi, Jiangsu Province 214028, People's Republic of China

⁴Collaborative Innovation Center of Advanced Microstructures, Nanjing University, Nanjing, 210093, People's Republic of China

E-mail: wzshen@sjtu.edu.cn

Received 14 January 2015, revised 5 February 2015

Accepted for publication 7 February 2015

Published 4 March 2015



CrossMark

Abstract

We report the realization of both excellent optical and electrical properties of nanostructured multicrystalline silicon solar cells by a simple and industrially compatible technique of surface morphology modification. The nanostructures are prepared by Ag-catalyzed chemical etching and subsequent NaOH treatment with controllable geometrical parameters and surface area enhancement ratio. We have examined in detail the influence of different surface area enhancement ratios on reflectance, carrier recombination characteristics and cell performance. By conducting a quantitative analysis of these factors, we have successfully demonstrated a higher-than-traditional output performance of nanostructured multicrystalline silicon solar cells with a low average reflectance of 4.93%, a low effective surface recombination velocity of 6.59 m s^{-1} , and a certified conversion efficiency of 17.75% on large size ($156 \times 156 \text{ mm}^2$) silicon cells, which is $\sim 0.3\%$ higher than the acid textured counterparts. The present work opens a potential prospect for the mass production of nanostructured solar cells with improved efficiencies.

Keywords: multicrystalline silicon solar cells, nanostructures, improved performance, large size, morphology modification

(Some figures may appear in colour only in the online journal)

1. Introduction

Multicrystalline silicon solar cells constitute the largest part of the present photovoltaic market and are expected to stay dominant in the near future, due to the low manufacturing cost at the mass production level. However, effective light trapping technique is still lacking for multicrystalline wafers and the average reflectance (R_{ave}) of multicrystalline silicon solar cells with a quarter-wavelength antireflective coating is

about 10%. It is therefore of great interest to the industry to further reduce the optical loss in order to increase the conversion efficiency (EFF). Recently, silicon nanostructures have attracted great attentions because of their excellent antireflection and light trapping effect [1–4], which make them promising candidates for reducing both the demand on the quality factor and quantity of silicon material [5]. But researchers have also encountered in these structures the difficulties of enhanced surface and Auger recombination at

the near surface [6, 7]. The degraded electrical properties counteract the benefits of optical enhancement in most attempts and lead to an inferior output performance of the nanostructured silicon solar cells when compared to the records of the conventional ones [6–20]. Therefore, the suppression of the carrier recombination turns out to be the primary focus for the performance improvement of the nanostructured multicrystalline silicon solar cells.

The usage of a passivation layer to saturate the surface defects and dangling bonds [17–21], implementation of light and shallow doping to lower the Auger recombination [7–9] as well as modification of nanostructures' morphology [9–16] have been proven to be effective methods to suppress the electrical loss. Among these three methods, surface morphology modification, including the control of the major structural parameters (filling ratio, periodicity, diameter, etc), is a simple and adaptable way to adjust the light absorption and surface area enhancement [22–25] in the present industrial manufacturing processes. Many groups have investigated surface morphology modification, providing valuable support for further improvement [9–16]. The EFF of silicon nanowire based solar cells has been optimized through controlling the aspect ratio and surface coverage of the nanostructure [13]. With an additional etching process to remove defects and regulate the density and height of nanohills, Xiao *et al* [16] have reached EFF of 17.46% on multicrystalline black silicon. Very recently, Liu *et al* [9] have reported the improvement of conversion EFF of multicrystalline silicon solar cells by incorporating reactive ion etching and acidic etching.

In this study, we report the realization of nanostructured multicrystalline silicon solar cells with 17.75% certified EFF on large area ($156 \times 156 \text{ mm}^2$) by a simple and industrially compatible technique, which is about 0.3% higher in absolute value than that of the conventional ones. The success lies in the surface morphology regulation to achieve a low electrical loss while keeping almost optimal optical performance. The surface modification is realized by Ag-catalyzed chemical etching [26–28] and subsequent NaOH modification to adjust the geometrical parameters of the as-grown nanostructured silicon wafers, i.e., the pore diameter, depth and the surface area enhancement ratio (A^F/A , where A^F is the front surface area of the nanostructured silicon wafer, and A is the surface area of the HF–HNO₃ textured wafer). We have found that R_{ave} decreases rapidly with increasing A^F/A for small A^F/A values and saturates for large ones, while the surface and Auger recombination increase linearly with the increase of A^F/A . The optimal value of A^F/A provides a low reflectance (4.93%) and low effective surface recombination velocity (6.59 m s^{-1}), and thus the highest output performance. Since both the growth of silicon nanostructures and the fabrication of nanostructured multicrystalline silicon solar cells have been carried out in the present industrial manufacturing processes, the present work opens a potential prospect for the mass production of nanostructured solar cells with higher-than-traditional conversion efficiencies.

2. Experimental details

Silicon nanopores were synthesized on one side of p-type ($1 \sim 3 \Omega \text{ cm}$, B doped, $190 \mu\text{m}$) solar-grade multicrystalline silicon wafers with a large area of $156 \times 156 \text{ mm}^2$ by Ag-catalyzed chemical etching and subsequent NaOH modification [26–28]. The wafers were first cleaned under standard RCA process and textured with hydrofluoric acid (HF) aqueous and nitric acid (HNO₃) solution. Then the acid textured wafers were paired in a back-to-back manner and immersed in a mixture of 0.005 mol L^{-1} HF aqueous and 0.001 mol L^{-1} silver nitrate (AgNO₃) solution for 90 s to ensure that only one side of each wafer was wrapped with silver nanoparticles. Ag-catalyzed acid etching was carried out in a 1:5:10 mixture of 40% HF: 30% hydrogen peroxide (H₂O₂): H₂O at room temperature for different etching times. Afterwards, in order to totally remove a nanoporous silicon layer which was produced during Ag-catalyzed acid etching process, all the wafers were immersed in 1 wt% NaOH solution for a certain time to yield nanopore structures. Finally, these wafers were dipped into HNO₃ aqueous solution to remove silver nanoparticles and rinsed with deionized water for several times.

We divided the samples into five series A, B, C, D and E corresponding to the different Ag-catalyzed chemical etching times of 30, 60, 120, 240 and 360 s, respectively. Samples in each series were further divided into subgroups by the duration ratio of their alkaline modification and the Ag-catalyzed chemical etching. Each subgroup has eight samples for reliable statistics. For example, B1.0 denotes the eight samples prepared by 60 s of Ag-catalyzed chemical etching followed by 60 s of alkaline-solution modification.

For solar cell fabrication, all the wafers were subjected to phosphorus diffusion using oxychloride (POCl₃) as the dopant source at 850 °C to form the p–n junction. Afterward the wafer edges were etched and the phosphosilicate glass was removed by 10% HF solution, resulting in a sheet resistance around $85 \Omega \text{ sq}^{-1}$. Then, a SiN_x layer (with a thickness of around 80 nm and a refractive index n of 2.15) was grown by plasma-enhanced chemical vapor deposition (PECVD). Finally, all the wafers went through the same processes of Al back-surface-field formation, screen-printing of front and back electrode, and electrode metallization.

The morphologies of the nanopore structures were examined by field emission scanning electron microscopy (FE-SEM, FEI SIRION 200). The effective minority carrier lifetime of the nanostructured silicon wafers (with nanostructure on one side and passivated by SiN_x layers on both sides) was acquired by using the quasi-steady state photoconductance decay method (WT1200A, Semilab). Both the optical reflectance and the external quantum efficiency (EQE) measurements were performed in the 300–1100 nm wavelength range by QEX10 (PV Measurements). The current–voltage characteristics of the nanostructure based silicon solar cells were measured at standard test conditions (an irradiation intensity of 1000 W m^{-2} , AM 1.5G and a temperature of $25 \pm 0.5 \text{ }^\circ\text{C}$).

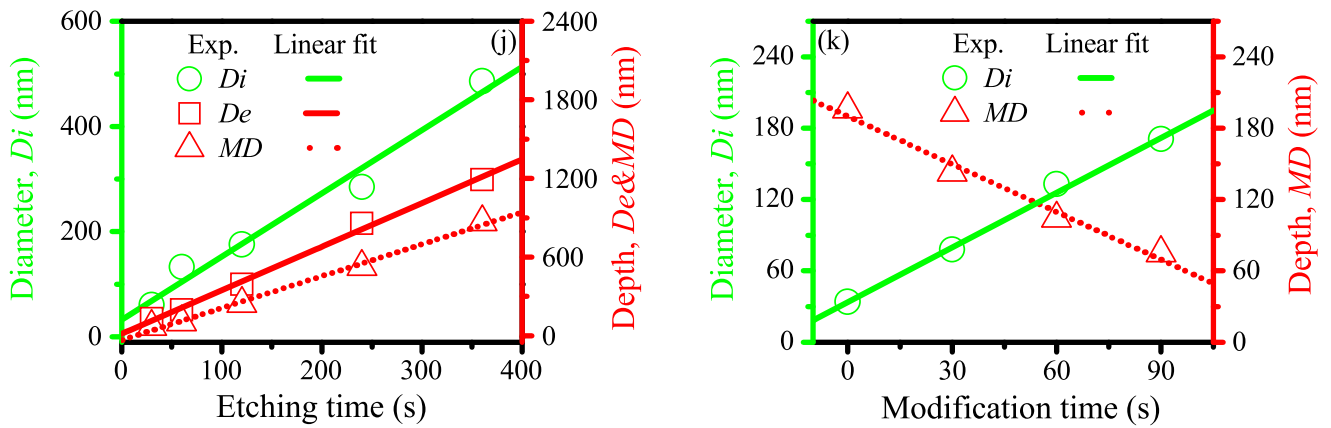
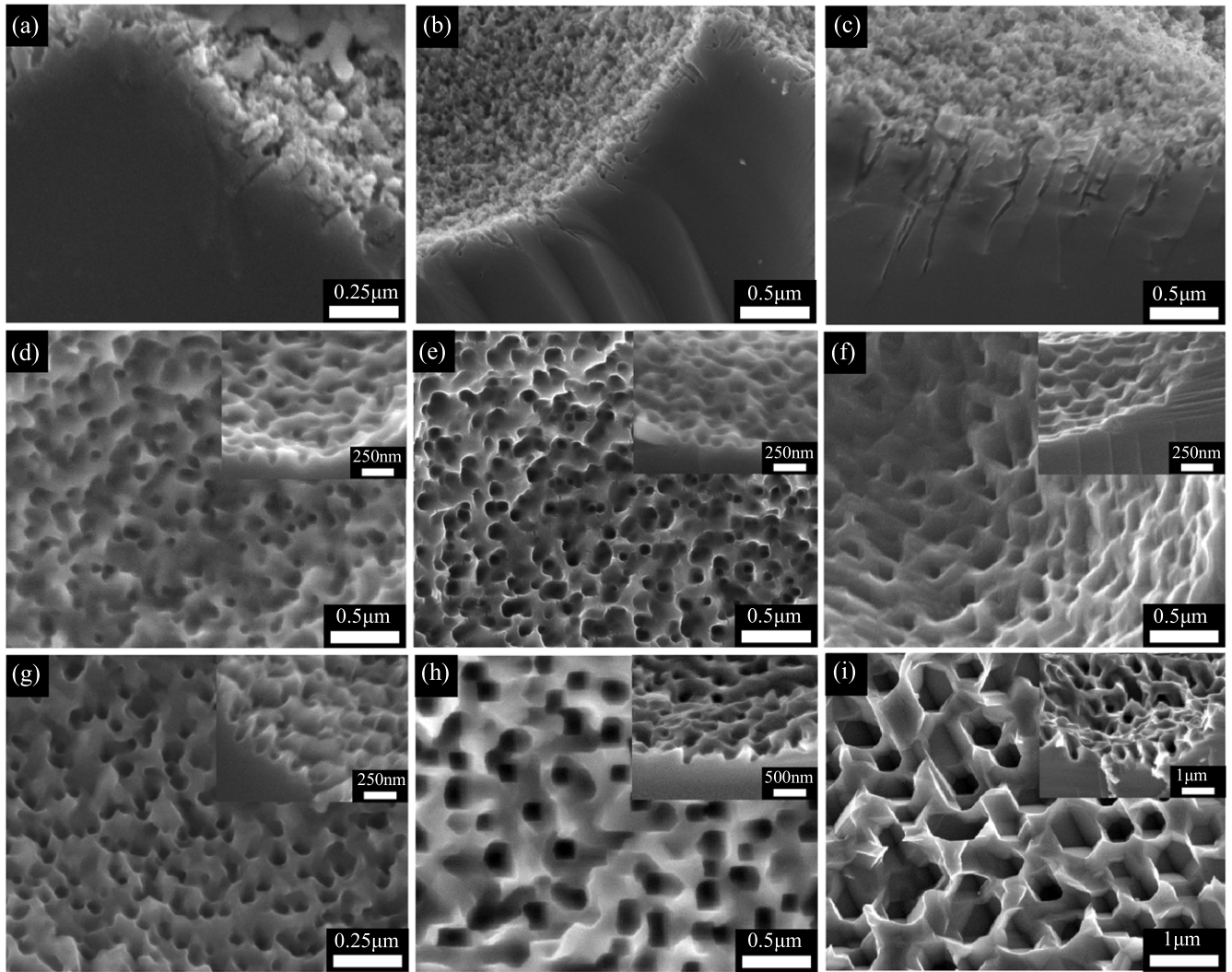


Figure 1. (a)–(c) Cross-sectional SEM images of series A0, C0 and E0, respectively. (d)–(i) SEM images of series B0.5, B1.0, B1.5, A1.0, C1.0 and E1.0 respectively, and the inset is the corresponding cross-sectional view. (j) Dependence of the measured average diameter D_i (green circles) and average depth MD (red triangles) of series A1.0, B1.0, C1.0, D1.0 and E1.0 on etching time, together with the dependence of the measured average depth De (red squares) of series A0, B0, C0, D0 and E0. (k) Dependence of the measured average diameter D_i (green circles) and average depth MD (red triangles) of series B0, B0.5, B1.0, B1.5 on the alkaline modification time. The scatters refer to experimental data and the lines denote the linear fit results.

Table 1. Average geometrical parameters deduced from SEM observations, i.e., diameter, depth and period, the calculated surface area enhancement ratio A^F/A by assuming the nanopore structures as equally distributed vertical nanopores, and average electrical parameters with errors (standard deviations), i.e., the open circuit voltage (V_{OC}), short circuit current (I_{SC}), fill factor (FF), efficiency (EFF), and extracted reverse saturation current (I_0), of different series of nanostructured solar cells and the acid textured counterparts (Ref., $A^F/A = 1.00$).

	A^F/A	Diameter (nm)	Depth (nm)	Period (nm)	V_{OC} (mV)	I_{SC} (A)	FF (%)	EFF (%)	I_0 (pA)
Ref.	1.00	—	—	—	626.0 ± 1.0	8.65 ± 0.02	77.78 ± 0.35	17.30 ± 0.08	263
B1.5	1.86	171	75	216	622.0 ± 0.7	8.70 ± 0.02	77.96 ± 0.16	17.33 ± 0.08	309
A1.0	2.15	61	69	107	621.0 ± 0.7	8.71 ± 0.02	78.48 ± 0.27	17.38 ± 0.10	322
B1.0	2.30	133	104	183	621.0 ± 1.6	8.76 ± 0.02	78.10 ± 0.20	17.47 ± 0.13	324
B0.5	2.64	78	143	146	619.0 ± 1.2	8.70 ± 0.01	77.93 ± 0.05	17.28 ± 0.06	347
C1.0	3.43	176	243	235	617.0 ± 0.5	8.61 ± 0.01	78.58 ± 0.29	17.14 ± 0.07	371
D1.0	4.77	285	525	353	614.0 ± 0.6	8.58 ± 0.03	78.44 ± 0.15	16.98 ± 0.09	416
E1.0	5.17	486	867	563	612.0 ± 1.2	8.52 ± 0.02	78.53 ± 0.24	16.84 ± 0.08	446

3. Controllable surface area enhancement

Figures 1(a)–(c) compare the typical cross-sectional SEM images of the three representative series A0, C0, and E0, respectively. Without the alkaline modification, it exhibits the cone-shaped nanopores on the acid textured silicon wafer surface surrounded with nanoporous silicon. Chartier *et al* [26] have observed similar SEM images of samples fabricated in a mixture of 1:4 (molar ratio) HF and H_2O_2 etching solution for 20 s. We have further found that the top diameter of the cone-shaped nanopores is insensitive to the etching time and is about 30 nm while the average nanopore depth D_e rises linearly with the etching time at a rate of $\sim 3.32 \text{ nm s}^{-1}$, as shown by the plot of figure 1(j) (red squares).

Figures 1(d)–(f) show the effect of the alkaline modification time by the SEM images of series B0.5, B1.0, and B1.5, respectively, and the inset is the corresponding cross-sectional view. Nanoporous silicon is dissolved and the diameter of the silicon nanopores enlarges while their depth decreases with increasing alkaline modification time, which is similar to previous results [12]. As plotted in figure 1(k), the average diameter D_i (green circles) and average depth MD (red triangles) both exhibit excellent linear behaviors with the modification time, giving etching rates of ~ 1.55 and 1.34 nm s^{-1} , respectively. It can be concluded that the role of the alkaline solution includes: (1) dissolving the nanoporous silicon to facilitate the formation of p–n junction in the phosphorus diffusion process [27]; (2) controlling the morphology of the silicon nanostructures through enlarging their diameter and reducing their depth, thus decreasing the surface area enhancement ratio A^F/A .

Figures 1(g)–(i) further present the SEM images of another three representative series A1.0, C1.0, and E1.0, respectively, and the inset is the corresponding cross-sectional view. As is shown in figure 1(j), under the same duration ratio of the Ag-catalyzed chemical etching and alkaline modification, the average diameter D_i (green circles) and depth MD (red triangles) change linearly with the etching time, giving the etching rates of ~ 1.20 and 2.43 nm s^{-1} , respectively.

From figure 1, we demonstrate that the depth of the final silicon nanopores is determined by both the Ag-catalyzed acid and the alkaline treatment while their diameter is only related

to the alkaline modification time. Since the surface area enhancement ratio A^F/A is related to the diameter and the depth of the nanopores, we can therefore tailor A^F/A of the as-grown nanostructured silicon wafer by controlling the two kinds of etching time. We have estimated the enhancement ratio A^F/A by assuming the nanopore structures as equally distributed vertical nanopores. Table 1 lists the average diameter, depth and period of each sample from the SEM observation, where the A^F/A ratios for all the samples in the present study have been deduced. As expected, A^F/A is found to decrease with the increase of the alkaline modification time and increase with the prolonged Ag-catalyzed chemical etching time. In short, we have realized the ability to regulate A^F/A of the as-grown nanostructured silicon wafer with diameter and depth changing from tens to hundreds of nanometers.

4. Reflectance characteristics

We start from the influence of the different surface area enhancement ratio A^F/A on the optical properties of nanopore structured wafers. In figure 2(a) we show the reflectance spectrum of each series over the wavelength range of 300–1100 nm, and the data of the acid textured wafer ($A^F/A = 1.00$) is also given for comparison. The as-grown silicon nanopore structures apparently demonstrate better antireflection characteristics than the acid textured wafer over the entire spectral range. This is due to the formation of a continuous gradient of refractivity which is desirable for suppressing the optical reflection [4]. Moreover, the reflectance is found to decrease with increasing enhancement ratio A^F/A (or increasing diameter and depth). Our results are consistent with that demonstrated by Sun *et al* [29], where lower reflectance is observed on deeper subwavelength structures due to the more gradual change of the refractive index between air and the nanostructured silicon surface. We have plotted in figure 2(c) (red squares) the average reflectance (R_{ave}) of each series weighted over the AM 1.5G solar spectrum in the range of 300–1100 nm. The dependence of R_{ave} on the variation of the enhancement ratio A^F/A is evident, e.g., the difference of R_{ave} between $A^F/A = 1.86$ and A^F/A

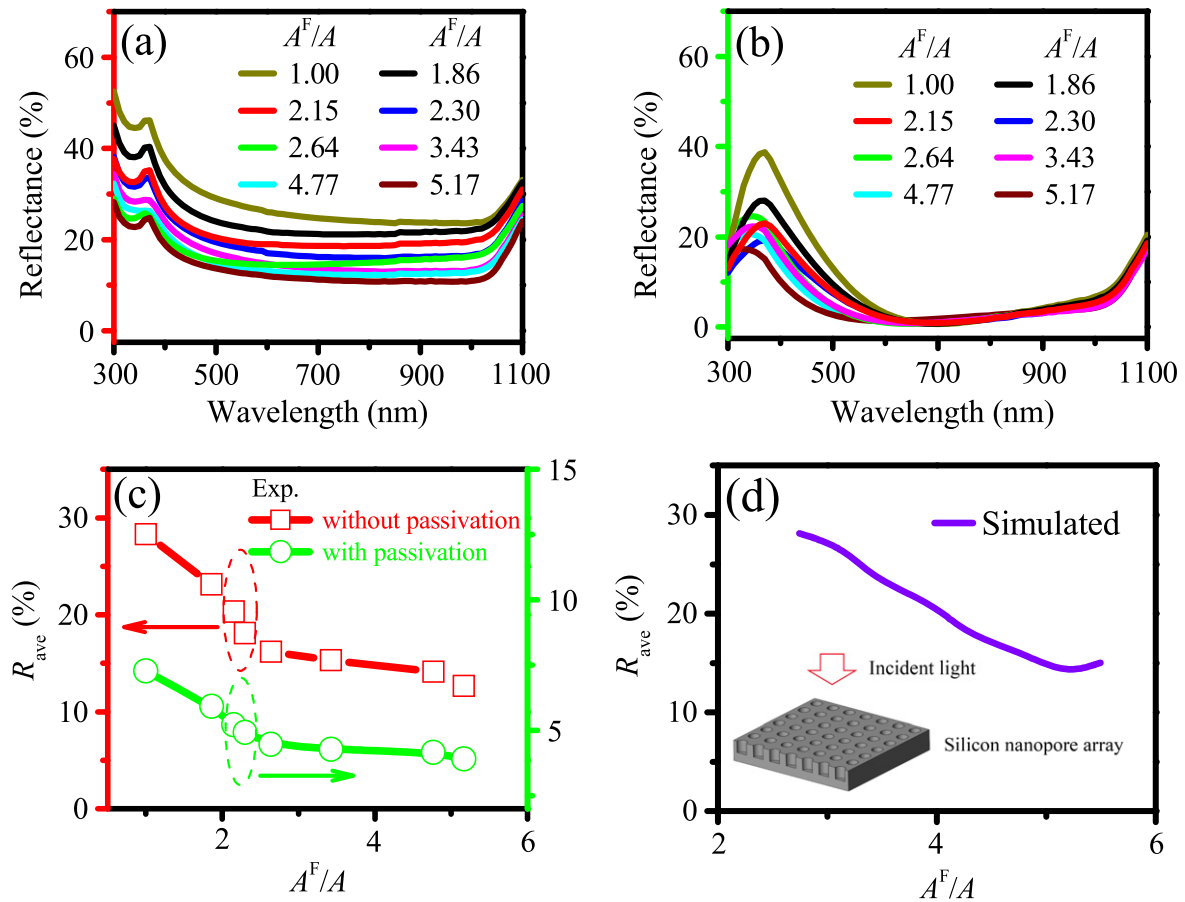


Figure 2. Experimental reflectance spectra of the different series of nanopore structured silicon wafers (a) without and (b) with a SiN_x passivation layer in the wavelength range of 300–1100 nm, together with the data of the acid textured wafer ($A^F/A = 1.00$) for comparison. (c) Relationship between the average reflectance R_{ave} and the surface area enhancement ratio A^F/A , obtained by weighting over the AM 1.5 G solar spectrum in the range 300–1100 nm. (d) FDTD simulated R_{ave} without SiN_x passivation layer versus A^F/A . The inset is the schematic simulation diagram where the array dimensions (pore diameter and depth, array period) are determined from their respective linear relations with the etching time as observed in the experiments (figure 1(j) and table 1).

$A = 5.17$ is 10.47% (R_{ave} of $A^F/A = 1.86$ and 5.17 are 23.13% and 12.66%, respectively). Nevertheless, the average reflectance R_{ave} decreases rapidly with increasing A^F/A for A^F/A values smaller than 2.64, while further increasing A^F/A above 2.64 only shows little reduction in R_{ave} .

We have also investigated the surface reflectance of both the nanostructured and acid textured silicon wafers coated with a SiN_x passivation layer (~ 80 nm with n of 2.15 by PECVD), as shown in figure 2(b). Compared to the acid textured wafer, the nanopore structured wafers exhibit lower reflectance in the wavelength range of 300–600 nm. However, the presented spectra of each series are quite similar to each other in the wavelength range from 600 to 1100 nm and notably decrease in comparison with the uncoated case in figure 2(a) due to the additional antireflection effect offered by the passivation layer. Obviously, the combination of the nanopore structure and SiN_x layer could provide excellent light trapping over a wide wavelength range, e.g., R_{ave} is decreased from 23.13% to 5.92% for $A^F/A = 1.86$ and 5.17 when the SiN_x layer is applied. In addition, the difference of R_{ave} between $A^F/A = 1.86$ and $A^F/A = 5.17$ is 2.01% (R_{ave} of $A^F/A = 1.86$ and 5.17 are 5.92% and 3.91%, respectively). This

shows that the passivation layer greatly diminishes the discrepancy of R_{ave} amongst samples with different A^F/A s. R_{ave} of each series shown in figure 2(b) is also illustrated in figure 2(c) (green circles), which shows similar trend as the uncoated case discussed above, only with much smaller values.

To deep understand the optical properties of this nanopore structure, we have performed finite-difference time-domain (FDTD) simulations to acquire R_{ave} of periodic nanopore arrays (without SiN_x passivation layers) on flat surfaces, where the array dimensions (pore diameter and depth, array period) are determined from their respective linear relations with the etching time as observed in the experiments (figure 1(j) and table 1). The simulated results in figure 2(d) exhibit an approximate linear relation between increasing A^F/A and decreasing R_{ave} , and R_{ave} saturates for higher A^F/A values, which is consistent with the experimental observations in figure 2(c). This correlation is attributed to two physical origins: First, as A^F/A increases from 2.7 to 5.5 in figure 2(d), the corresponding pore dimensions increase from ~ 100 to ~ 500 nm, approaching that of the central wavelength of the solar spectrum. The comparable structural

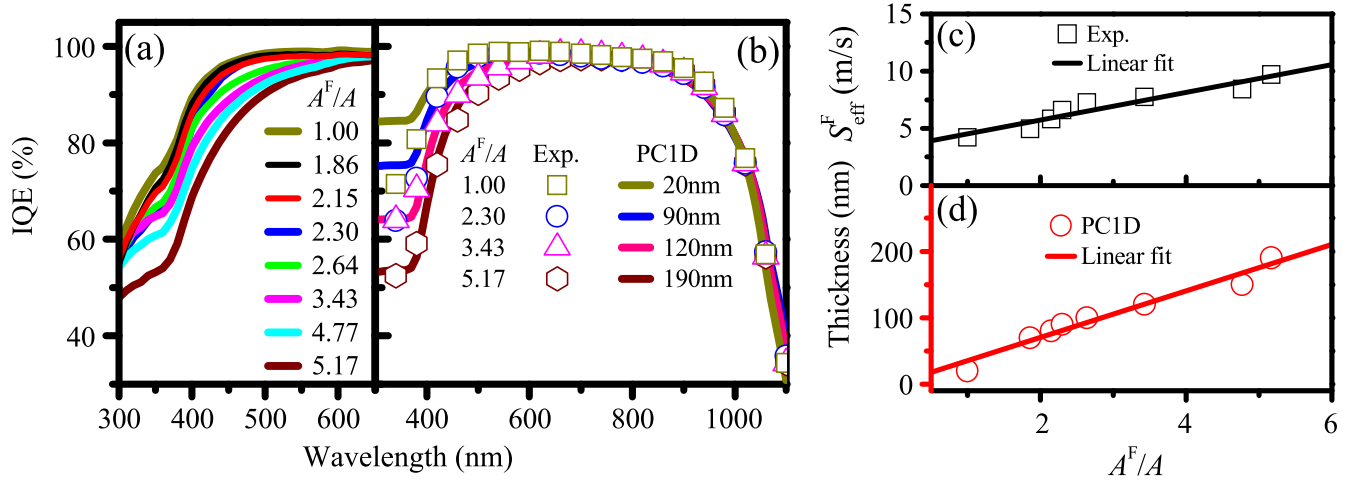


Figure 3. (a) Experimental average IQE spectra of each series in the wavelength range of 300–650 nm. (b) Experimental average IQE spectra (scatters) and the calculated IQE results from the PC1D simulations based on the ‘dead layer’ model (curves) of series B1.0 ($A^F/A = 2.30$), C1.0 ($A^F/A = 3.43$) and E1.0 ($A^F/A = 5.17$) in the wavelength range of 300–1100 nm, together with the data of the acid textured wafer ($A^F/A = 1.00$). (c) Measured effective surface recombination velocity S_{eff}^F and (d) thickness of the ‘dead layer’ of each series versus A^F/A , where the scatters refer to (c) experimental and (d) simulated data, together with the linear fit results.

size to the incident wavelength induces stronger scattering of light and thus provides better antireflection properties [30]; second, the factor A^F/A is a direct indicator of the area percentage of the inner walls of the nanopores. As this factor goes up, the multiple reflection by the nanopore walls is enhanced, which further lowers the reflectance [31]. However, the most important discrepancy between the experiments and the simulations is that the linear decreasing of R_{ave} in the experiments occurs at much smaller values of A^F/A compared to the simulated ones, e.g., the saturation point moves from ~ 5.3 in the simulations to ~ 2.5 in the experiments. Such difference is caused by the acid textured surfaces of the silicon wafers in the experiments, which provide a baseline of scattering of the incident light and thus allow a comparable R_{ave} to be achieved for smaller A^F/A s. This phenomenon, together with the use of an antireflection coating, significantly lowers the requirement of the surface roughness (A^F/A) for achieving an ideal optical performance, which is extremely beneficial for maintaining a good electrical behavior of the solar cells.

5. Carrier recombination

We now focus on the influence of the surface area enhancement on charge collection EFF by investigating the internal quantum efficiency (IQE) of the nanostructured silicon solar cells. The IQE of these solar cells has been derived from the EQE characteristics via $\text{IQE} = \text{EQE}/(1 - R)$, where R is the reflectance presented in figure 2(b). Figure 3(a) shows the average IQE spectra in the range of 300–650 nm for the cell series of A1.0, B0.5, B1.0, B1.5, C1.0, D1.0 and E1.0 and the data of the acid textured wafer cells are also given for comparison (each subgroup has eight samples). Although the IQE in the short wavelength range declines with the increase of the enhancement ratio A^F/A , an indication of an enhanced Auger

and surface recombination, it remains almost unchanged for small A^F/A values as embodied by samples B1.5 ($A^F/A = 1.86$), A1.0 ($A^F/A = 2.15$), and B1.0 ($A^F/A = 2.30$), as well as the acid textured ones ($A^F/A = 1.00$).

We have measured the effective minority carrier lifetime (τ_{eff}), in order to have a deep insight into the mechanism of the IQE reduction. Generally, τ_{eff} could be expressed as [7]

$$\frac{1}{\tau_{\text{eff}}} = \frac{1}{\tau_{\text{bulk}}} + (S_{\text{eff}}^F + S_{\text{eff}}^B)/d, \quad (1)$$

where τ_{bulk} is the bulk Shockley–Read–Hall lifetime (in our case, $\tau_{\text{bulk}} = 24.52 \mu\text{s}$), S_{eff}^F and S_{eff}^B are the effective surface recombination velocities (including surface recombination and near surface Auger recombination) at the front surface and at the back surface, respectively, and d is the wafer thickness (in our case, $d = 190 \mu\text{m}$). S_{eff}^F and S_{eff}^B are equal for the acid textured wafer, since it is textured and passivated symmetrically. In addition, we assume a same S_{eff}^B value for all sample series since their back surfaces underwent the same PECVD- SiN_x passivation, and only the front surfaces are processed differently. Therefore, we can yield S_{eff}^F for each series and the results are plotted in figure 3(c) (black squares), where S_{eff}^F rises nearly linearly with the surface area enhancement ratio A^F/A at a rate of $\sim 1.20 \text{ m s}^{-1}$ and reaches as high as 9.69 m s^{-1} for the nanostructured wafer of E1.0 ($A^F/A = 5.17$). We can attribute the enhanced S_{eff}^F to the increasing surface area [6].

It has been noted that the Auger recombination channel is the dominant contributor to S_{eff}^F under high doping concentrations (sheet resistance below $90 \Omega \text{ sq}^{-1}$) due to excess doping through the nanostructured surface, which contributes to the reduction of IQE in the short wavelength range [7]. Such dominance is confirmed by our simulations using the one dimensional device program PC1D, where the IQE curves of the nanostructured solar cells are unable to be modeled by setting the surface recombination velocity and

bulk lifetime. Therefore, we analyze the mechanism of the IQE reduction by the Auger recombination known as the ‘dead layer’ model [10]. Note that, though the actual nanostructured silicon solar cells cannot be directly constructed by PC1D, but it can be equivalently simulated by using planar solar cell with ‘dead layer’ model, together with optical and electrical parameters (surface reflectance, base doping concentration, series resistance and bulk lifetime, etc.) extracted from the actual devices. We have treated the nanopore structure as a low lifetime ‘dead layer’ by setting a doping density of $\sim 2 \times 10^{20} \text{ cm}^{-3}$ in the PC1D simulations, and varied the thickness of this layer to acquire the corresponding IQE curves. The ‘dead layer’ thickness of the acid textured wafer cells is also simulated by PC1D program.

Figure 3(b) exhibits the four representative simulations (curves) for the dead layer thicknesses of 20, 90, 120 and 190 nm, which match well with the experimental data (scatters) of samples with $A^F/A = 1.00, 2.30, 3.43$ and 5.17 , respectively, in the wavelength range of 300–1100 nm. By comparing the simulated IQE curves with the experimental ones, we have found that the degrading performance of the nanostructured samples with increasing A^F/A values can be approximated by a series of planar cells with increasing dead layer thicknesses. It is shown in figure 3(d) (red circles) that the ‘dead layer’ thickness rises linearly with increasing enhancement ratio A^F/A , indicating increasing Auger recombination. Such behavior is due to the dependence of the Auger recombination on the volume of the heavily doped emitter, which is proportional to the surface area under the same diffusion process. This result agrees well with our previous work that the thickness of the nanowire ‘dead layer’ goes up with increasing nanowire length (or enhancement ratio A^F/A) [17].

In short, our result shows that the Auger recombination dominates in heavily doped nanostructures, and that it has a linear relationship with A^F/A . On the other hand, the surface recombination is also proportional to the surface area, although in our case its contribution is less pronounced. Hence, A^F/A has to be restricted to relatively small values, in order to maintain a satisfactory electrical property of the nanostructured cells with low Auger and surface recombination.

6. Cell performance

We further show the output performance of the nanostructured silicon solar cells to evaluate the comprehensive impact of the surface area enhancement ratio A^F/A discussed above. The experimental average conversion EFF of each series is illustrated in figure 4(a) by black circles with error bars (standard deviations). From figure 4(a), we can see that the average EFF grows with the increase of A^F/A and reaches its highest at $A^F/A = 2.30$ with average EFF = 17.47%, i.e., an absolute increase of 0.17% over that of the acid textured ($A^F/A = 1.00$) counterparts (17.30%), while further increasing A^F/A above 2.30 only leads to a rapid reduction in

average EFF. The superiority of the series B1.0 cells ($A^F/A = 2.30$) can be attributed to a trade-off between the antireflection gain and blue IQE loss, that is a low reflectance (4.93%), together with a low effective surface recombination velocity (6.59 m s^{-1}) and a small ‘dead layer’ thickness (90 nm). As mentioned above, each subgroup of cells has eight samples, figure 4(b) exhibits the EFF distribution of the four representative series of cells with $A^F/A = 1.00, 2.30, 3.43$ and 5.17 , respectively. We can see that the highest EFF of $A^F/A = 2.30$ cells is 17.76%, which has also been measured independently by TÜV Corporation (TÜV Report No. 15067482.001) with open circuit voltage (V_{OC}) of 0.6291 V, short circuit current (I_{SC}) of 8.667 A, fill factor (FF) of 79.2% and EFF as high as 17.75% under AM 1.5G illumination, as shown in figure 4(c). This indicates the potential for the practical fabrication of large size nanostructured silicon solar cells with satisfactory conversion EFF.

For a more detailed comparison, we have illustrated the average electrical parameters for each series in table 1. We notice that I_{SC} increases with increasing A^F/A for A^F/A values smaller than 2.30, while further increasing A^F/A above 2.30 only shows rapid reduction in I_{SC} . The variation of I_{SC} with A^F/A shows a similar trend as that of the average EFF discussed above. For small values of A^F/A , R_{ave} decreases rapidly which leads to the increase in I_{SC} , indicating the vital role of R_{ave} on determining the EFF in these cases. The highest I_{SC} ($A^F/A = 2.30$) is about 0.11 A larger than that of the reference one, which guarantees the average EFF increase by 0.17%. Moreover, although samples of series B0.5, C1.0, D1.0 and E1.0 possess similar reflectance ($\sim 4\%$), their I_{SC} s differ notably. I_{SC} decreases with the increase of the enhancement ratio A^F/A , e.g., I_{SC} of series C1.0, D1.0 and E1.0 is even less than that of the acid textured ones, clearly showing that the increasing surface and Auger recombination have outweighed the benefit of optical absorption, leading to the reduction in EFF. This demonstrates that for large A^F/A values, carrier recombination plays an important role on determining the EFF. In addition, we have also calculated the saturation current (I_0) [32], which is listed in table 1. We notice that I_0 gradually increases with the enhancement ratio A^F/A , indicating an increasing recombination in the nanopore structures. These results agree well with our discussion in section 5 about the carrier recombination.

We have also shown the simulated EFF of the nanopore structured silicon solar cells based on the ‘dead layer’ analogy, as is shown in figure 4(a) (red curve), which is in good accordance with the experimental results. The simulated results exhibit that the EFF grows with the increase of A^F/A and reaches its highest at $A^F/A = 2.40$ with EFF = 17.57%, i.e., an absolute increase of 0.27% over that of the acid textured ones (17.30% as simulated by PC1D), while further increasing A^F/A above 2.40 only leads to a rapid reduction in EFF. As is discussed above, there exists an optimal value of A^F/A that maximizes the EFF of the nanostructured cells due to the competing influence of A^F/A on the optical and the electrical properties. It is therefore of paramount importance to choose an appropriate A^F/A in cell fabrication.

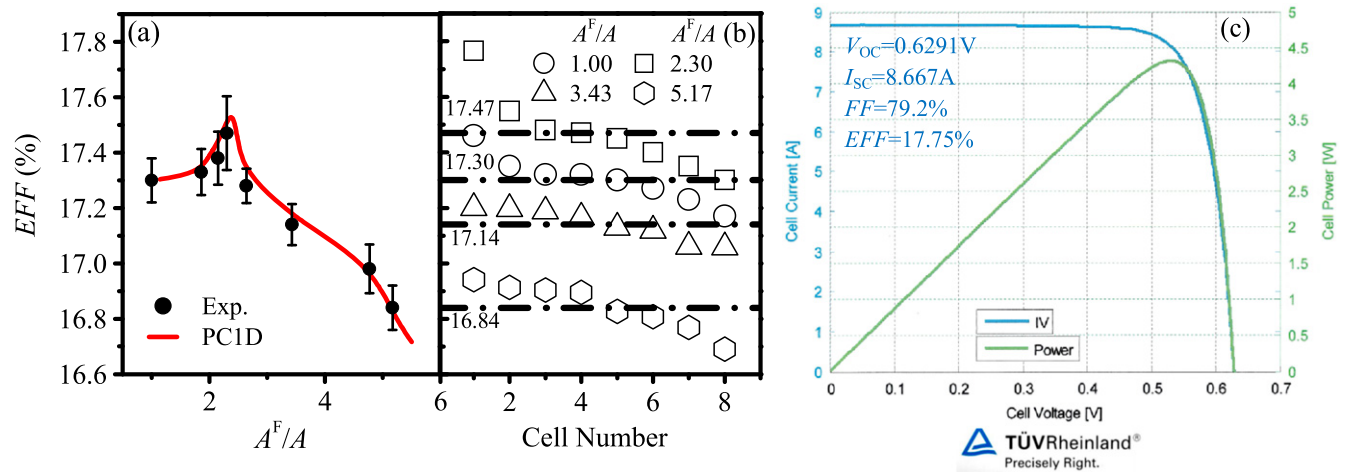


Figure 4. (a) Experimental (black circles with error bars, i.e., standard deviations) and PC1D simulated (curves) average conversion efficiency (EFF) of each series versus A^F/A . (b) EFF distribution of the four representative series of cells with $A^F/A = 1.00$ (circles), 2.30 (squares), 3.43 (triangles) and 5.17 (hexagons), respectively. (c) Current–voltage characteristics of the optimal cell of B1.0 measured independently by TÜV Corporation (TÜV Report No. 15067482.001) under AM 1.5G illumination.

Finally, it should be noted that in this investigation, all the experiments were conducted in the actual production lines of one of the largest solar cell producers (Suntech) with fully mass-production-compatible technologies (e.g., we have chosen SiN_x passivation instead of more complicated ones). The EFF of $\sim 17.5\%$ directly represents the current conversion efficiencies of real-life mass-produced mc-Si solar cells. The resultant EFF improvement ($\sim 0.3\%$) is not only industrially significant, but also represents a turning point in the long pursuit of nanostructure application in solar cells where most previous attempts have only shown inferior cell performance than the conventional counterparts. Furthermore, the average output performance of our best nanostructured silicon solar cells ($A^F/A = 2.30$, average EFF = 17.47%) can still be improved in certain aspects. The surface enhancement ratio A^F/A could be more elaborately regulated since R_{ave} of the highest EFF ($A^F/A = 2.30$) is still a little high (4.93%). For further promotion of EFF, a simple way is to adopt the light-and-shallow doping together with a denser electrode grid to avoid high sheet resistance [8], or to increase the characteristic nanoscale dimension to adjust the phosphorous distribution in the nanostructures [8] and minimize the unfavorable Auger recombination. Atomic-layer-deposited Al_2O_3 can also be used to significantly suppress the Auger and surface recombination via the field effect passivation [17–21].

7. Conclusions

In summary, we have presented a simple method to modify silicon nanostructures' surface morphology and adjust the surface area enhancement ratio A^F/A by Ag-catalyzed chemical etching and subsequent NaOH modification, during which the diameter and depth of the nanostructures can be effectively changed from tens to hundreds of nanometers. We have found that the average reflectance R_{ave} s of samples

without and with SiN_x passivation layer both decline rapidly with the increase of A^F/A for small A^F/A values and saturate for large ones, and that the passivation layer greatly diminishes the discrepancy of R_{ave} amongst samples with different A^F/A s, which significantly lowers the requirement of the surface roughness (A^F/A) for achieving an ideal optical performance. In addition, both the surface and Auger recombination have a linear relationship with A^F/A while the Auger recombination dominates in heavily doped nanostructures. Through a detailed investigation of the competing influence of A^F/A on the optical and the electrical properties, we have successfully achieved an EFF of 17.75% on nanostructured multicrystalline solar cells, where the optimal value of A^F/A ($A^F/A = 2.30$) provides a low reflectance of 4.93% and a low effective surface recombination velocity of 6.59 m s^{-1} . The present work opens a potential prospect for the fabrication of large size ($156 \times 156 \text{ mm}^2$) nanostructured multicrystalline solar cells with higher-than-traditional efficiencies in the present industrial manufacturing processes. Further improvement of the cell performance can be realized with the back surface textured (i.e., double-side texture) so as to randomize the directions of the reflected light, together with the doping scenario optimized for the enhanced open-circuit voltage.

Acknowledgments

This work was supported by the Natural Science Foundation of China (61234005, 11174202 and 11474201).

References

- [1] Hu L and Chen G 2007 Analysis of optical absorption in silicon nanowire arrays for photovoltaic applications *Nano Lett.* **7** 3249–52

- [2] Tsakalakos L *et al* 2007 Strong broadband optical absorption in silicon nanowire films *J. Nanophotonics* **1** 013552
- [3] Han S E and Chen G 2010 Toward the lambertian limit of light trapping in thin nanostructured silicon solar cells *Nano Lett.* **10** 4692–6
- [4] Branz H M, Yost V E, Ward S, Jones K M, To B and Stradins P 2009 Nanostructured black silicon and the optical reflectance of graded-density surfaces *Appl. Phys. Lett.* **94** 231121
- [5] Kayes B M, Atwater H A and Lewis N S 2005 Comparison of the device physics principles of planar and radial p–n junction nanorod solar cells *J. Appl. Phys.* **97** 114302
- [6] Peng K Q, Xu Y, Wu Y, Yan Y J, Lee S T and Zhu J 2005 Aligned single-crystalline Si nanowire arrays for photovoltaic applications *Small* **1** 1062–7
- [7] Oh J, Yuan H C and Branz H M 2012 An 18.2%-efficiency black-silicon solar cell achieved through control of carrier recombination in nanostructures *Nat. Nanotechnology* **7** 743–8
- [8] Wang Y, Liu Y P, Lai T, Liang H L, Li Z L, Mei Z X, Zhang F M, Kuznetsov A and Du X L 2013 Selective nano-emitter fabricated silver assisted chemical etch-back for multicrystalline solar cells *RSC Adv.* **3** 15483–9
- [9] Liu S Y *et al* 2014 Improvement of conversion efficiency of multicrystalline silicon solar cells by incorporating reactive ion etching texturing *Sol. Energy Mater. Sol. Cells* **127** 21–6
- [10] Yuan H C, Yost V E, Page M R, Stradins P, Meier D L and Branz H M 2009 Efficient black silicon solar cell with a density-graded nanoporous surface: optical properties, performance limitations, and design rules *Appl. Phys. Lett.* **95** 123501
- [11] Toor F, Branz H M, Page M R, Jones K M and Yuan H C 2011 Multi-scale surface texture to improve blue response of nanoporous black silicon solar cells *Appl. Phys. Lett.* **99** 103501
- [12] Yue Z H *et al* 2014 Large-scale black multi-crystalline silicon solar cell with conversion efficiency over 18% *Appl. Phys. A* **116** 683–8
- [13] Huang B R, Yang Y K and Yang W L 2014 Efficiency improvement of silicon nanostructure-based solar cells *Nanotechnology* **25** 035401
- [14] Zhong S H, Liu B W, Xia Y, Liu J H, Liu J, Shen Z N, Xu Z and Li C B 2013 Influence of the texturing structure on the properties of black silicon solar cell *Sol. Energy Mater. Sol. Cells* **108** 200–4
- [15] Chen H Y *et al* 2014 Enhanced performance of solar cells with optimized surface recombination and efficient photon capturing via anisotropic-etching of black silicon *Appl. Phys. Lett.* **104** 193904
- [16] Xiao G, Liu B W, Liu J H and Xu Z 2014 The study of defect removal etching of black silicon for solar cells *Mater. Sci. Semicond. Process.* **22** 64–8
- [17] Lin X X, Hua X, Huang Z G and Shen W Z 2013 Realization of high performance silicon nanowire based solar cells with large size *Nanotechnology* **24** 235402
- [18] Wang W C, Lin C W, Chen H J, Chang C W, Huang J J, Yang M J, Tjahjono B, Huang J J, Hsu W C and Chen M J 2013 Surface passivation of efficient nanotextured black silicon solar cells using thermal atomic layer deposition *ACS Appl. Mater. Interfaces* **5** 9752–9
- [19] Repo P, Benick J, Vähänissi V, Schön J, Gastrow G V, Steinhäuser B, Schubert M C, Hermle M and Savin H 2013 N-type black silicon solar cells *Energy Procedia* **38** 866–71
- [20] Dou B F, Jia R, Sun Y, Li H F, Chen C, Jin Z and Liu X Y 2013 Surface passivation of nano-textured silicon solar cells by atomic layer deposited Al₂O₃ films *J. Appl. Phys.* **114** 174301
- [21] Huang Z G, Hua S H, Hua X, Lin X X, Kong X Y, Dai N and Shen W Z 2014 An effective way to simultaneous realization of excellent optical and electrical performance in large-scale si nano/microstructures *Prog. Photovolt., Res. Appl.* doi:10.1002/pip.2506
- [22] Han S E and Chen G 2010 Optical absorption enhancement in silicon nanohole arrays for solar photovoltaics *Nano Lett.* **10** 1012–5
- [23] Gjessing J, Sudbo A S and Marstein E S 2011 Comparison of periodic light-trapping structures in thin crystalline silicon solar cells *J. Appl. Phys.* **110** 033104
- [24] Li J S, Yu H Y, Wong S M, Li X C, Zhang G, Lo P G Q and Kwong D L 2009 Design guidelines of periodic Si nanowire arrays for solar cell application *Appl. Phys. Lett.* **95** 243113
- [25] Xie Z, Wang W, Qin L X, Xu W J and Qin G G 2013 Optical absorption characteristics of nanometer and submicron a-Si:H solar cells with two kinds of nano textures *Opt. Express* **21** 18043–52
- [26] Chartier C, Bastide S and Lévy-Clément C 2008 Metal-assisted chemical etching of silicon in HF–H₂O₂ *Electrochim. Acta* **53** 5509–16
- [27] Tsujino K, Matsumura M and Nishimoto Y 2006 Texturization of multicrystalline silicon wafers for solar cells by chemical treatment using metallic catalyst *Sol. Energy Mater. Sol. Cells* **90** 100–10
- [28] Shi J W, Xu F, Zhou P H, Yang J, Yang Z B, Chen D S, Yin Y F, Chen D D and Ma Z Q 2013 Refined nano-textured surface coupled with SiN_x layer on the improved photovoltaic properties of multi-crystalline silicon solar cells *Solid-State Electron.* **85** 23–7
- [29] Sun C H, Min W L, Linn N C, Jiang P and Jiang B 2007 Templated fabrication of large area subwavelength antireflection gratings on silicon *Appl. Phys. Lett.* **91** 231105
- [30] Bohren C F and Huffman D R 1983 *Absorption and Scattering of Light by Small Particles* (New York: Wiley) chapter 5
- [31] Liu J, Zhang T C, Dong G Q, Zhang X S, Wang B, Liao Y X and Yi F T 2013 Fabrication and antireflection properties of solar cells with pyramid-nanohole texture by caesium chloride lithography *J. Phys. D: Appl. Phys.* **46** 375302
- [32] Gray J L 2003 *Handbook of Photovoltaic Science and Engineering* ed A Luque and S Hegedus (New York: Wiley) chapter 3